Johannes Hoffmann, Clint Hansen, Walter Maetzler, and Gerhard Schmidt*

A Concept for 6D Motion Sensing with Magnetoelectric Sensors

https://doi.org/10.1515/cdbme-2022-1115

Abstract: Active magnetic motion sensing relies on a combination of magnetic sensors and actuators to indirectly sense a time-varying change in position and orientation. Based on our previous work on a 1D setup with magnetoelectric (ME) sensors, we introduce a concept for a full 6D sensing system, which is positioned as a modular setup for human movement pattern capture with regard to neurodegenerative diseases. In this paper, we implemented an inverse model based on ideal triaxial sensors and coils. We then included results from the previous experiments to estimate the prospective performance in a physical setup. We obtained a spatial error of a few cm and approx. $10°$ with focus on superimposed sinusoidal movements of 1, 5, and $10\,\mathrm{Hz}$.

Keywords: magnetoelectric sensors, motion sensing, motion tracking, AC magnetic fields, artificial fields, magnetic fields

1 Introduction

Analyses of human movement patterns are of high relevance in both diagnosis and therapy of movement disorders like Parkinson's disease. While lab-bound optical motion capture is the gold standard, wearable sensors (mainly inertial measurement units, IMUs) are emerging as an alternative. However, reliable and accurate computation of crucial motor markers like step length is challenging [1]. Potential candidates for supplemental data acquisition include time of arrival (ToA) [2] and magnetic [3] methods. The presented magnetic approach focuses on $3 \times 1\ \mathrm{mm}$ magnetoelectric cantilever sensors, which offer a magnetic noise of single digit $\mathrm{pT}/\sqrt{\mathrm{Hz}}$ in their first bending mode at $7.7\,\mathrm{kHz}$ [4]. Avoidance of conductive and ferromagnetic materials and the $1/r^3$ decay of magnetic dipole fields suggest to aim for small distributed sources and sensors with short distances. Such an approach relies on the ability to accurately separate the source signals even in the case of high bandwidth demands due to motion. In contrast to quasi-stationary localization approaches (e.g., [5]) that aim for a minimization of the spatial uncertainty, the temporal uncertainty (capturing higher frequency components) also is of great concern here. In [6], we demonstrated both the fundamental feasibility of a basic motion sensing system in a 1D setup as well as the ability to use frequency-division multiple access (FDMA) techniques to separate multiple sources. However, the physical setup was not able to reconstruct movements apart from very constraint scenarios. Therefore, we propose the use of 3D sensors as well as 3D coils for a full 6D motion sensing approach (Fig. 1). The fundamental setup contains a transmitter unit with signal generation for three coils and a receiver unit with preprocessing (band-limiting, equalizing), channel separation, and finally the dipole estimator that is the focus of this paper.

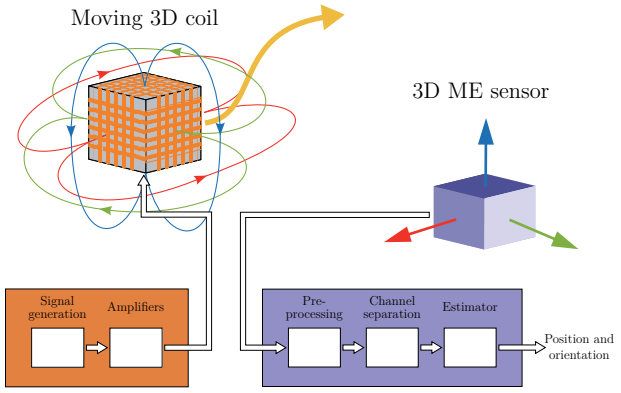

Fig. 1: Overview of the magnetoelectric motion sensing system.

2 Methods

2.1 Magnetic Dipole Approximation

Assuming a sufficient displacement, the vector field $\vec{\boldsymbol{b}}$ (magnetic flux density) of a short cylindric coil can be approximated as a dipole [7] with constant parameters aggregated in b_0 and the vector field directivity $\vec{\boldsymbol{\theta}}$. Here, the 3D sensor's position and orientation towards the coil (origin, normal vector in x direction) are described as a position vector $\vec{\boldsymbol{r}}$ (r: length, $\vec{\boldsymbol{e}}_\mathrm{r}$: normalized position vector) and a rotation matrix $\boldsymbol{R}$:

$$\vec{\boldsymbol{b}}(\vec{\boldsymbol{r}}, \boldsymbol{R}) = b_0 \, \frac{1}{r^3} \, \boldsymbol{R} \, \vec{\boldsymbol{\theta}}_\mathrm{x}(\vec{\boldsymbol{e}}_\mathrm{r}). \tag{1}$$

***Corresponding author: Gerhard Schmidt,** Institute of Electrical Engineering and Information Technology, Kiel University, Kaiserstr. 2, 24143 Kiel, Germany, gus@tf.uni-kiel.de
Johannes Hoffmann, Institute of Electrical Engineering and Information Technology, Kiel University, Kiel, Germany
Clint Hansen, Walter Maetzler, Department of Neurology, Kiel University, Kiel, Germany

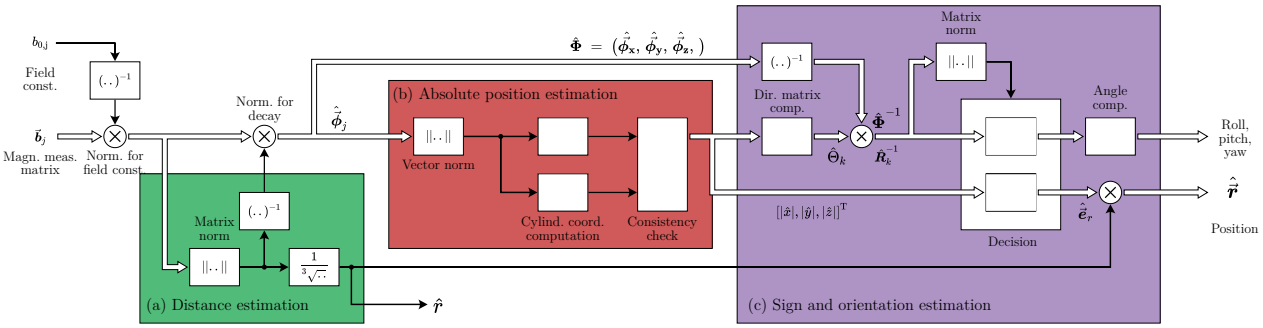

Fig. 2: Overview on the proposed inverse model for a 6D motion sensing approach.

The resulting equation system is only solvable for heavily constrained movements (e.g., 1D motion with fixed orientation) and otherwise under-determined with up to three unknowns for position and orientation each. In case of a 3D source comprised of three dipole sources (assuming ideal signal separation), $\vec{\boldsymbol{b}}$ is replaced by a 3×3 matrix $\boldsymbol{B}$:

$$\boldsymbol{B}(\vec{\boldsymbol{r}}, \boldsymbol{R}) = b_0 \, \frac{1}{r^3} \, \boldsymbol{R} \underbrace{\left[\vec{\boldsymbol{\theta}}_{\mathrm{x}}(\vec{\boldsymbol{e}}_{\mathrm{r}}),\ \vec{\boldsymbol{\theta}}_{\mathrm{y}}(\vec{\boldsymbol{e}}_{\mathrm{r}}),\ \vec{\boldsymbol{\theta}}_{\mathrm{z}}(\vec{\boldsymbol{e}}_{\mathrm{r}})\right]}_{\boldsymbol{\Theta}(\vec{\boldsymbol{e}}_{\mathrm{r}})}. \quad (2)$$

The directivity matrix $\boldsymbol{\Theta}(\vec{\boldsymbol{e}}_{\mathrm{r}})$ is symmetric with the components x, y and z of the normalized position vector $\vec{\boldsymbol{e}}_{\mathrm{r}}$:

$$\begin{aligned} \boldsymbol{\Theta}(\vec{\boldsymbol{e}}_{\mathrm{r}}) &= \frac{1}{2}\left(3\,\vec{\boldsymbol{e}}_{\mathrm{r}}\vec{\boldsymbol{e}}_{\mathrm{r}}^{\mathrm{T}} - I\right) \\ &= \frac{1}{2}\begin{pmatrix} 3x^2-1 & 3xy & 3xz \\ 3xy & 3y^2-1 & 3yz \\ 3xz & 3yz & 3z^2-1 \end{pmatrix}. \end{aligned} \quad (3)$$

The resulting equation system with nine (partly dependent) equations and six unknowns is the basis for the applied inverse approach to obtain both position and orientation.

2.2 Inverse Solution

The described approach for a 6D inverse model is comprised of three chained subsystems, depicted in Fig. 2 as (a), (b) and (c). We expect slightly different parameters for each coil, which are therefore denoted as $\hat{b}_{0,\mathrm{j}}$. These might be estimated beforehand based on coil characterization ($\hat{R}_j$: mean radius, $\hat{N}_j$: number of windings) and current measurements $\hat{I}_j$ according to:

$$\hat{b}_{0,\mathrm{j}} = \frac{\mu_0 \hat{N}_j \hat{R}_j^2}{2} \hat{I}_j. \quad (4)$$

2.2.1 Distance

As the first processing step, we obtain the distance-dependency $\hat{r}^3$ from the measured $\hat{\boldsymbol{B}}$ matrix which contains three vectors $\hat{\vec{\boldsymbol{b}}}_j$. The computation (from eq. 2) is straightforward as it can be shown that the spectral norm of both rotation and directivity matrix is 1:

$$\frac{1}{\hat{r}^3} = \left\| \left[\frac{\hat{\vec{\boldsymbol{b}}}_{\mathbf{x}}}{\hat{b}_{0,\mathrm{x}}},\ \frac{\hat{\vec{\boldsymbol{b}}}_{\mathbf{y}}}{\hat{b}_{0,\mathrm{y}}},\ \frac{\hat{\vec{\boldsymbol{b}}}_{\mathbf{z}}}{\hat{b}_{0,\mathrm{z}}} \right] \right\|_2. \quad (5)$$

We introduce another normalization step to get the rotated directivity matrix $\hat{\boldsymbol{\Phi}}$, which is adjusted for both distance and coil parameters:

$$\hat{\boldsymbol{\Phi}} = \left[\hat{\vec{\boldsymbol{\phi}}}_{\mathrm{x}},\ \hat{\vec{\boldsymbol{\phi}}}_{\mathrm{y}},\ \hat{\vec{\boldsymbol{\phi}}}_{\mathrm{z}},\right] = \hat{r}^3 \left[\frac{\hat{\vec{\boldsymbol{b}}}_{\mathbf{x}}}{\hat{b}_{0,\mathrm{x}}},\ \frac{\hat{\vec{\boldsymbol{b}}}_{\mathbf{y}}}{\hat{b}_{0,\mathrm{y}}},\ \frac{\hat{\vec{\boldsymbol{b}}}_{\mathbf{z}}}{\hat{b}_{0,\mathrm{z}}} \right]. \quad (6)$$

2.2.2 Absolute Position Components

After normalization, the estimated position might be described by a position vector of unit length with the components $\hat{x}$, $\hat{y}$ and $\hat{z}$. The multiplication of the individual vectors $\hat{\vec{\boldsymbol{\phi}}}_j$ with the rotation matrix does not affect its length $\hat{\phi}_j$ (vector norm), which we compute next. The vector norm of the normalized magnetic dipole field is depicted in Fig. 3. E.g., for the x coil, $\hat{\phi}_{\mathrm{x}}$ can be attributed to a specific axial ($\hat{x}_{\mathrm{x}}$) and radial ($\hat{\rho}_{\mathrm{x}}$) displacement:

$$|\hat{x}_{\mathrm{x}}| = \sqrt{\frac{4\hat{\vec{\boldsymbol{\phi}}}_{\mathrm{x}}{}^2 - 1}{3}} \quad \text{and} \quad |\hat{\rho}_{\mathrm{x}}| = \sqrt{\frac{4 - 4\hat{\vec{\boldsymbol{\phi}}}_{\mathrm{x}}{}^2}{3}}. \quad (7)$$

However, the angular component and the signs are ambiguous due to rotational symmetry and the square-root operator, respectively. We repeat this step for each of the coils.

Fig. 3 displays each coil's contribution as a circle. In the ideal scenario, there is one point where all three circles intersect in each octant of the coordinate system. The graphic also

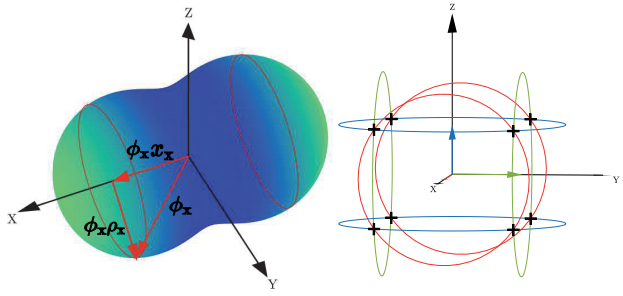

Fig. 3: Orientation-dependent vector norm of the magnetic dipole.

highlights that one of the components is redundant as it can be indirectly computed from the axial and radial displacements of the other two. To support subsequent processing steps, we identify the component with the highest inconsistency (direct vs. indirect) and replace it based on the vector length.

2.2.3 Ambiguity and Orientation

Due to the symmetry of $\hat{\boldsymbol{\Phi}}$ (cf. (3)), ambiguity can not be completely avoided. Therefore, we exclude negative x values. There remain four possible octants in the coordinate system (i.e., four sign combinations for y and z). For each combination, we compute a matrix $\vec{\boldsymbol{\Theta}}^k$ according to (3). With (2) and the previously computed matrix $\hat{\boldsymbol{\Phi}}$ instead of $\boldsymbol{B}$ we get:

$$\hat{\boldsymbol{\Phi}} = \hat{\boldsymbol{R}}_k \hat{\boldsymbol{\Theta}}_k \;\Rightarrow\; \hat{\boldsymbol{R}}_k^{-1} = \hat{\boldsymbol{\Theta}}_k \, \hat{\boldsymbol{\Phi}}^{-1}. \tag{8}$$

We compute the norm of each transformation matrix candidate that transforms $\hat{\boldsymbol{\Theta}}_k$ into $\hat{\boldsymbol{\Phi}}$. As a rotation matrix does not affect the length of a vector multiplied with it, we can select the matrix with the norm closest to 1. Based on this decision, we set the signs of the position and compute the angles.

2.3 Parameters of the Physical Setup

To this point, we outlined a theoretical approach that works error-free with simulated data, but does not take neither time nor noise into account. Thus, we included anticipated flaws of our prospective physical setup. As the actual sensors have a certain form-factor, there is some spacing between their sensor elements required. This causes a deviation from the point assumption for the ideal 3D sensor. Therefore, we assumed a virtual center of the 3D sensor from which each sensor deviates by $1\,\mathrm{cm}$ in the direction of its sensitive axis. The actually available bandwidth for magnetic input signals (i.e., caused by movement-induced modulation) was set to $100\,\mathrm{Hz}$ (matched filter length of $10\,\mathrm{ms}$). This corresponds to an additive input noise of approx. $0.5\,\mathrm{nT}$ for each sensor (assuming resting sensor, moving coil [6]). For perspective, the simulated 3D coil ($3\times$ 100 windings, $13.5\,\mathrm{mm}$ mean radius, $400\,\mathrm{mA}$) produces low double digit nT at a distance of $50\,\mathrm{cm}$. We applied zero-phase lowpass filtering to the retrieved position/angle signals (Butterworth, 2nd order, $20\,\mathrm{Hz}$).

3 Results

Fig. 4 shows the simulation results with the color scheme displayed above. The ground truth is depicted in a darker shade of the same color.

As we focus on the performance of the approach in motion, we defined an appropriate motion scenario: The simulated position was comprised of two sinusoidal signals (x: $20\,\mathrm{cm}$ amplitude at $1\,\mathrm{Hz}$, y: $5\,\mathrm{cm}$ at $10\,\mathrm{Hz}$). We applied similar signals for the angles (roll: $5°$ at $5\,\mathrm{Hz}$, pitch: $45°$ at $1\,\mathrm{Hz}$).

Fig. 4 **a** shows the position estimation compared to the actual position. The y component was quite noisy. The z component was affected by a low frequency oscillation, which could clearly be seen in the corresponding error plot (Fig. 4 **b**). The mean absolute error (MAE) was $1.2\,\mathrm{cm}$ for x, $3.6\,\mathrm{cm}$ for y, $1.7\,\mathrm{cm}$ for z, and $7\,\mathrm{mm}$ for the overall distance. We also focused on the spectral properties of the x and y component (FFT, $5\,\mathrm{s}$, 1024 Points), which are depicted in Fig. 4 **c**. The low frequency component ($1\,\mathrm{Hz}$) was accurately restored, the $10\,\mathrm{Hz}$ signal was significantly attenuated (factor 2).

Similar considerations can be made for the obtained orientation estimation (Fig. 4 **d**). As the error plot (Fig. 4 **e**) highlights, pitch estimation was most accurate with an MAE of $6°$ with roll and pitch close to $10°$. In the spectral plot (Fig. 4 **f**), both expected peaks at $1\,\mathrm{Hz}$ and $5\,\mathrm{Hz}$ were clearly visible while there were some additional peaks (e.g., $10\,\mathrm{Hz}$).

4 Conclusion

In this paper, we simulated the behavior of a magnetoelectric 6D motion sensing system. We considered the static performance in terms of a spatial error, but also the ability of the proposed setup to capture a weaker, superimposed motion at a higher frequency. Overall, the accuracy of the position (and esp. distance) estimation seemed appropriate for further research regarding the prospective use case as a supplemental sensor in clinical application. While the restored $10\,\mathrm{Hz}$ frequency component was significantly attenuated, there might still be some value in identifying the frequency itself.

However, the deviation from the ideal 3D sensor was actually more critically (esp. for orientation) than the noise in this

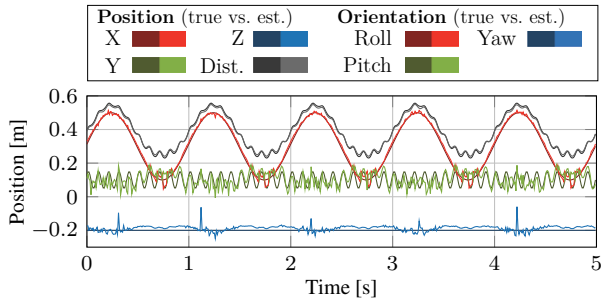

(a) Position: Estimation vs. ground truth.

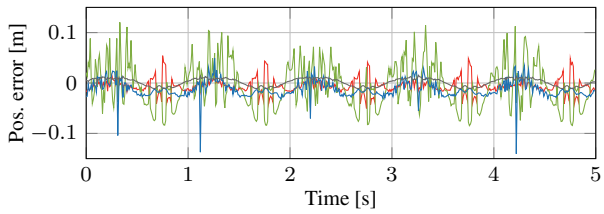

(b) Position error.

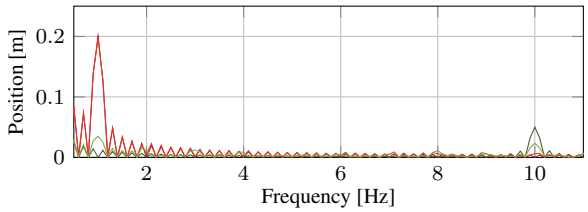

(c) Position (spectral): Estimation vs. ground truth.

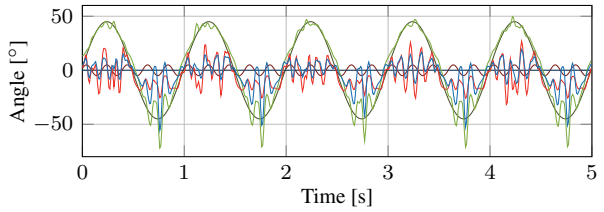

(d) Angles: Estimation vs. ground truth.

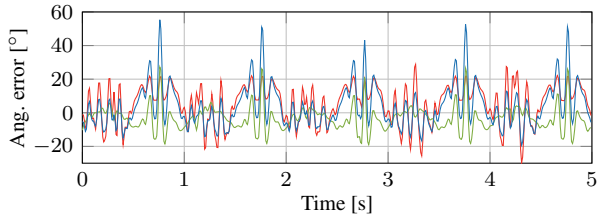

(e) Angle error.

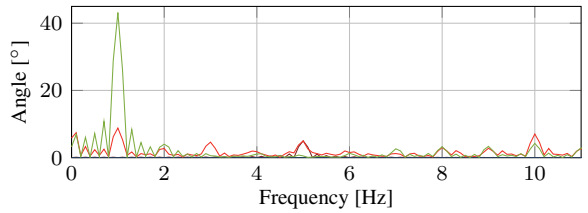

(f) Angles (spectral): Estimation vs. ground truth.

Fig. 4: Simulation results for sinusoidal movements.

specific simulation. This is probably related to the fact that the distance between the sensor elements is (too) large in comparison to the sensor coil distance. This became clear from the undesired sinusoidal signal components which were mostly interference from the 10 Hz translatory movement. Currently, the naive dipole estimation approach does not really account for it, which might be improved in combination with a better redundancy exploitation of the dipole geometry. The assumed distance between the sensor elements was based on currently available sensors, which might by overcome with dedicated 3D sensors. We also expect significant improvements by applying a tracking algorithm (e.g., Kalman) to exploit inertia.

Author Statement

Research funding: This work was supported by the German Research Foundation (Deutsche Forschungsgemeinschaft, DFG) through the project B9 of the Collaborative Research Centre CRC 1261 “Magnetoelectric Sensors: From Composite Materials to Biomagnetic Diagnostics”. Conflict of interest: Authors state no conflict of interest. Informed consent: Informed consent has been obtained from all individuals included in this study. Ethical approval: The research related to human use complies with all the relevant national regulations, institutional policies and was performed in accordance with the tenets of the Helsinki Declaration, and has been approved by the authors’ institutional review board or equivalent committee.

References

[1] Díez LE, Bahillo A, Otegui J, Otim T. Step Length Estimation Methods Based on Inertial Sensors: A Review. IEEE Sens J 2018;18(17):6908-6926.

[2] Xu C, He J, Zhang X, Zhou X, Duan S. Towards Human Motion Tracking: Multi-Sensory IMU/TOA Fusion Method and Fundamental Limits. Electronics. 2019; 8(2):142.

[3] Roetenberg D, Slycke PJ, Veltink, PH. Ambulatory Position and Orientation Tracking Fusing Magnetic and Inertial Sensing. IEEE Trans Biomed Eng 2007;54(5):883-890.

[4] Elzenheimer E, Bald C, Engelhardt E, Hoffmann J, Hayes P, Arbustini J, et al. Quantitative Evaluation for Magnetoelectric Sensor Systems in Biomagnetic Diagnostics. Sensors. 2022;22(3):1018.

[5] De Angelis G, Pasku V, De Angelis A, Dionigi M, Mongiardo M, Moschitta A, et al. An Indoor AC Magnetic Positioning System. IEEE Trans Instrum Meas 2015;64(5):1267-1275.

[6] Hoffmann J, Elzenheimer E, Bald C, Hansen C, Maetzler W, Schmidt G. Active Magnetoelectric Motion Sensing: Examining Performance Metrics with an Experimental Setup. Sensors. 2021;21(23):8000.

[7] Paperno E, Plotkin A. Cylindrical induction coil to accurately imitate the ideal magnetic dipole. Sens Actuator A Phys 2004;112:248-252.